Microscopic Mechanisms of Local Interfacial Resistive Switching in LaMnO 3+δ

Benjamin Meunier, Dolors Pla, Raquel Rodriguez-Lamas, Michel Boudard, Odette Chaix-Pluchery, Eugenie Martinez, Nicolas Chevalier, Carmen Jiménez, Mónica Burriel, Olivier Renault

ACS APPLIED ELECTRONIC MATERIALS

Article

Cite This: ACS Appl. Electron. Mater. 2019, 1, 675−683

pubs.acs.org/acsaelm

Microscopic Mechanisms of Local Interfacial Resistive Switching in $LaMnO_{3+\delta}$

Benjamin Meunier,*[,†] Dolors Pla,[†] Raquel Rodriguez-Lamas,[†] Michel Boudard,[†] Odette Chaix-Pluchery,[†] Eugénie Martinez,[‡] Nicolas Chevalier,[‡] Carmen Jiménez,[‡] Mónica Burriel,*[,†] and Olivier Renault[‡]

[†]Univ. Grenoble Alpes, CNRS, Grenoble INP, LMGP, 38000 Grenoble, France

[‡]Univ. Grenoble Alpes, CEA, LETI, 38000 Grenoble, France

Supporting Information

ABSTRACT: Manganite perovskites exhibit promising resistive switching properties, for which the understanding of the related microscopic physicochemical changes taking place is still rather scarce. In this work the resistance of a $LaMnO_{3+\delta}$ thin film has been locally tuned within a range of 2 orders of magnitude using conductive atomic force microscopy. With the use of X-ray photoemission electron microscopy it has been possible to simultaneously unravel composition and work function modification related to changes in the $LaMnO_{3+\delta}$ resistance state. The resistance change is found to be triggered by oxygen ions drifting to the surface, where they remain adsorbed. Concomitant to this oxygen displacement, the Mn oxidation state is reduced from +3.6 to +3.1, while the work function decreases by 0.28 eV. We discuss the effect of these physicochemical modifications on the conduction mechanism, which is in agreement with a space-charge-limited conduction (SCLC) mechanism where the current is restrained by the density of traps at the interface. We show that the resistive switching in the material can be described as a change of the transport regime from a trap-free to a trap-controlled SCLC, depending on the oxygen content in the material.

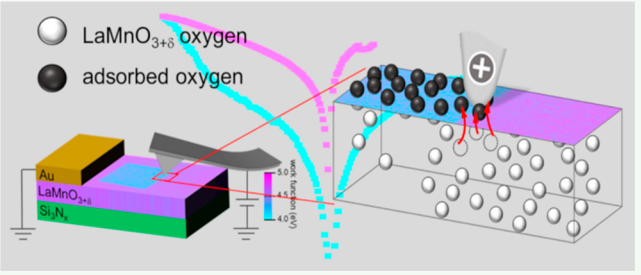

KEYWORDS: *resistive switching, lanthanum manganites, X-ray photoemission electron microscopy, c-AFM, MOCVD*

INTRODUCTION

The rising demand for data storage and miniaturized electronic devices pushes the present flash technology to its limits.[1,2] New oxide-based resistive switching memories have emerged as alternative nonvolatile resistive random access memories (RRAMs) to increase the density data storage as well as enhance the devices endurance and retention.[3] Among the plethora of oxide structures exhibiting resistive switching (RS) response, perovskites such as $(Pr,Ca)MnO_3$,[4] $SmNiO_3$,[5] $SrZrO_3$,[6−8] and $LaSrMnO_3$,[9,10] as well as the thoroughly studied $SrTiO_3$,[11] have already shown memristive behavior.

Among the number of different mechanisms that can lead to RS in perovskites, the valence change mechanism (VCM), which controls the behavior of ionic−electronic resistive switches, is one of the most common and promising ones.[12] This VCM can occur through the creation of conducting oxygen vacancy filaments between the two metal electrodes (filamentary VCM) or the accumulation of oxygen vacancies at the electrode−oxide interface (interface-type VCM).[13] Several chemical and physical processes have been reported to be involved in the VCM-based memristive characteristics in perovskites, for example, redistribution of point defects, oxygen exchange with the environment, charge-carrier transport at interfaces, and electronic trapping or tunneling effects.[14] However, few works are devoted to correlate and disentangle them due to the difficulty in obtaining accurate compositional, structural, and electronic information with nanometric resolution in the regions of interest.[15−20] Direct experiments correlating the local surface chemistry, nanostructure, and electronic transport modifications taking place during interfacial RS in perovskites are yet missing. This lack of understanding of the coupled physicochemical processes is particularly acute for the case of polycrystalline perovskites integrated in silicon substrates in the thin film form.

Mixed-valence manganites have attracted much attention over the past decades due to their unique electric (e.g., Mott−Hubbard interaction, double exchange interaction, metal-to-insulator transitions), optical (e.g., spectral weight transfer in optical conductivity), magnetic (e.g., magnetic phase transitions, magnetic ordering temperature), and transport (e.g., colossal magnetoresistance effect, Jahn−Teller distortion effect, ion conduction) properties derived from their large capability of defect chemistry engineering.[21,22] In particular, properties are strongly correlated to the Mn valence state and

Received: January 16, 2019
Accepted: April 18, 2019
Published: April 18, 2019

DOI: 10.1021/acsaelm.9b00030
ACS Appl. Electron. Mater. 2019, 1, 675−683

the oxygen stoichiometry; for example the metal−insulator transition in $La_{0.8}Sr_{0.2}MnO_3$ induced by oxygen vacancies.[20,23,24] Among the mixed-valence manganite materials, thin films of $LaMnO_{3\pm\delta}$ have been extensively studied as cathode materials for solid oxide fuel cells due to their high oxygen reduction catalytic activity.[25] As many manganites, $LaMnO_{3\pm\delta}$ thin films can be obtained over a large composition range, particularly by varying the oxygen content. The oxygen deficiency (i.e., $LaMnO_{3-\delta}$) occurs via the creation of oxygen vacancies in the material, whereas the apparent oxygen excess is ascribed to the formation of La or/and Mn cation vacancy sites (i.e., $La_{1-x}\square_x$, $Mn_{1-y}\square_yO_3$, viz. $LaMnO_{3+\delta}$), where $\square$ represents cation vacancies and charge neutrality remains fulfilled thanks to the presence of a mixture of Mn^{3+}/Mn^{4+} oxidation states.[23,26−28] Because of steric effects, it is commonly admitted that $LaMnO_{3+\delta}$ cannot present interstitial oxygen in its structure.

This work delves into the physicochemical changes occurring at the $LaMnO_{3+\delta}$ (LMO) surface during reversible interfacial RS. We combine conductive atomic force microscopy (c-AFM), X-ray photoemission electron microscopy (XPEEM), and Raman spectroscopy to elucidate the compositional, structural, and electrical modifications involved in the switching response. The 25 nm thick dense LMO thin films grown on a $SiN_x/SiO_2/Si$ heterostructure were switched from an initial low resistance state (LRS) to a high resistance state (HRS) using c-AFM. Being able to selectively switch micrometer-scale areas at different resistance states, the local work function, the lattice system, and the chemical state of all LMO constituent elements at surface level have been solved and directly related to the resistive states. The results reported here are of crucial importance enabling a better understanding of interfacial-type RS in polycrystalline manganite films and advancing toward the development of new nanoengineered perovskite-based memristive devices.

EXPERIMENTAL SECTION

Material Deposition. LMO films ∼25 nm thick were grown by pulsed injection metal−organic chemical vapor deposition (PI-MOCVD) on top of single crystal (100)-oriented silicon chips, covered by a stress free bilayer composed of 100 nm thick thermal SiO_2 and 300 nm thick SiN_x grown by low-pressure chemical vapor deposition. An homogeneous solution of 2,2,6,6-tetramethylheptane-3,5-dionate metal precursors, i.e., $La(thd)_3$ and $Mn(thd)_3$, was prepared using a $[La(thd)_3]/[Mn(thd)_3]$ ratio equal to 2. The optimum growth conditions for these dense polycrystalline films were at 973 K with a background O_2 pressure fixed to 5 Torr, using a pulse frequency of 2.5 Hz and 4000 pulses.

Instrumentation. Grazing incidence X-ray diffraction (GIXRD) 2θ scans were performed using a Rigaku-Smartlab diffractometer equipped with a rotating anode to characterize the crystal structure of LMO films.

AFM and c-AFM were performed in a Dimension Icon from Bruker located in a nitrogen-filled glovebox (H_2O and O_2 content below 3 ppm). Highly p-doped diamond-coated Si tips (CDT-NCHR from Nanosensors) with a radius in the range 20−50 nm, a nominal spring constant of 80 N/m, and an electrical resistance of 6 kΩ were used for the RS measurements. The applied force on the surface of the film was set to the 0.3−0.9 μN range to ensure efficient electrical contact and low mechanical pressure (<1 GPa). Prior to the electrical measurements, the sample was heated at 390 K for 1 h to remove the moisture and ensure a clean LMO surface. Electrical measurements were performed inside the glovebox using a Keithley 2635B. The $I-V$ characteristics were studied by sweeping from zero to positive voltage, then to negative voltage, and back to zero (i.e., 0 V → 20 V → 0 V → −20 V → 0 V) at around ±600 mV/s and grounding a semi-infinite Au electrode located at ∼100 μm from the tip. It is worthy to mention that several $I-V$ measurements were performed at different distances from the semi-infinite top electrode to optimize the distance (i.e., ∼100 μm), ensuring a reproducible switching response and avoiding leakage currents to the Au electrode (which occurred for very short distances). The scanning c-AFM mode was used to change the resistance state in a micrometric area at the virgin LMO surface. The writing, erasing, and reading voltages used were +4, −6, and ±0.5 V, respectively, and a pulse duration of 0.5 s.

The study of the local structure changes was performed by Raman spectroscopy. Particularly, the variation of the Jahn−Teller effect with the Mn^{4+}/Mn^{3+} ratio was investigated for both resistance states. Raman spectra were collected at room temperature in a backscattering geometry using a Jobin Yvon/Horiba Labram spectrometer equipped with a liquid nitrogen cooled CCD detector. The 488 nm Ar^+ laser line with an incident power of ∼1.2 mW was used for excitation. The light was focused to a spot size of ∼1 μm in diameter by a ×100 objective. The Raman spectra were calibrated using a silicon reference spectrum at room temperature (theoretical position = 520.7 cm^{-1}).

The local surface analyses were performed by XPEEM with a high transmission, aberration-compensated energy filter (double hemispherical analyzer) and a focused monochromatic Al Kα source (1486.6 eV). This microscopic photoemission technique provides information about both the work function and the chemical state of specific elements from a given area of interest at the surface. For the local work function analyses, spectromicroscopy measurements were performed in which full field, energy-filtered images using secondary electrons are recorded. Photoelectron images were acquired within an energy range $E-E_F$ = 1.5−10 eV (0.025 eV energy steps and 4 s acquisition time per image). For the chemical state analysis, the instrument was switched to the microspectroscopic mode in which photoemission spectra were collected by closing a field aperture on either the HRS or the LRS region. Prior to the analysis, the LMO surface was cleaned under UHV for 25 s by gentle ion sputtering to selectively remove the adventitious carbon contamination without damaging the oxide surface. The sample was then transferred in a vacuum transport vessel to the XPEEM chamber. Secondary electron images were used to localize the area where c-AFM was previously performed.

Data Treatment of Photoemission Spectra. The following methodology was used to analyze the La 3d, O 1s, Mn 2p, and Mn 3s core level spectra recorded. A Shirley-type background was subtracted excluding the plasmon and Auger regions from the La 3d surrounding. Quantification was performed based on the La 3d, O 1s, and Mn 2p peaks. The manganese stoichiometry was calculated using the Mn 2p core level due to its better signal-to-noise ratio compared to the Mn 3s spectrum. The area of each contribution was normalized by the corresponding cross section of its core level,[29] the inelastic mean free path calculated for bulk LMO, and the transmission function of the analyzer. Peak fitting of La $3d_{5/2}$, O 1s, and Mn 3s was performed using the pseudo-Voigt function. Although this function does not separate the effect of the core-hole lifetime and instrumental broadening (since the width is the same for both Lorentzian and Gaussian contributions), it is commonly used and is considered as an accurate enough approximation for the compositional study of the LMO surface.

RESULTS AND DISCUSSION

Characterization of LMO Thin Film. The surface morphology of fully dense LMO thin films determined by AFM in the tapping mode is presented in Figure 1a. It shows grains of several tens of nanometers in diameter with a smooth surface morphology (roughness rms value ∼1.07 nm). The GIXRD pattern shown in Figure 1b, according to the 04-007-6350 file of the International Center for Diffraction Data (ICDD), as well as Raman spectra and high-resolution transmission electron microscopy (Figures S2 and S3 in the Supporting Information, respectively), reveal a single rhombo-

DOI: 10.1021/acsaelm.9b00030
ACS Appl. Electron. Mater. 2019, 1, 675−683

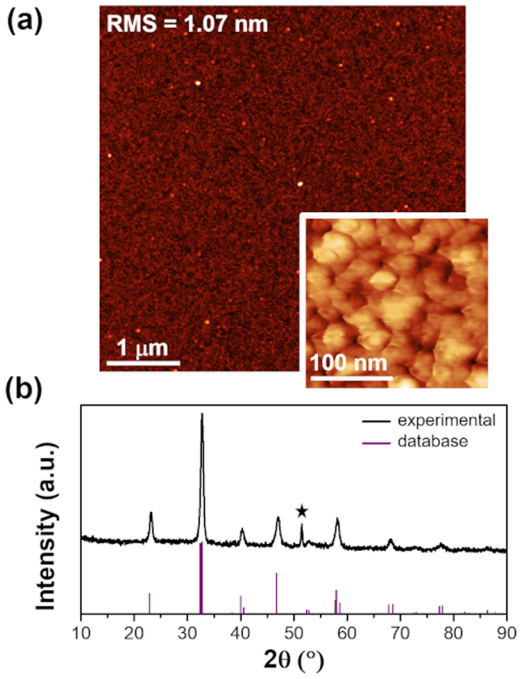

Figure 1. Thin film characterization of the $LaMnO_3/Si_3N_x/SiO_2/Si$ heterostructure by (a) 5 × 5 μm^2 AFM topographic image obtained in the tapping mode (inset: 250 × 250 nm^2) and (b) experimental GIXRD pattern (★: Si substrate) compared with the ICDD-04-007-6350 file of LMO ($La_{0.95}Mn_{0.95}O_3$, space group $R\bar{3}c$, a = 5.52419 Å, c = 13.33110 Å).

hedral phase of polycrystalline LMO without preferential orientation and with no secondary phase. Further details on the observed modifications in the Raman spectra and possible identification of phases (orthorhombic and rhombohedral) for LMO thin films with different oxygen content can be found in the work by Rodríguez-Lamas et al.[30] The cation stoichiometry of the film was determined by EDX as La/Mn = 1.02 (the corresponding SEM image in Figure S1).

Interfacial Resistive Switching of LMO Induced by c-AFM. Figure 2a presents a sketch of the fabricated Au/LMO/Si-based memristive heterostructure, while Figure 2b shows the hysteretic current−voltage (I−V) characteristics measured for LMO by cyclic voltammetry (the curve corresponds to the first sweep). LMO exhibits an asymmetric bipolar counter-eight-wise-type switching without requiring an electroforming step. In all cases noticeable differences were observed between the SET and RESET processes. An abrupt SET from LRS to HRS occurred for positive polarity at ∼6.5 V. Conversely, a gradual RESET was achieved by progressively decreasing the voltage in the negative polarity.

To analyze the electrical transport mechanisms, the logarithmic representation of the I−V curve is presented in Figure 2c. For negative voltage, the $\log(I)$−$\log(V)$ plot presents three linear regions with different slopes (m) characteristic of a space-charge-limited conduction (SCLC) mechanism.[31,32] At low voltage (region I) the thermal generation of free carriers inside the material dominates. As the voltage increases (region II), the density of injected carriers becomes larger than the thermally generated carriers, and the SCLC regime, controlled by the density of trapped charges (m > 2), appears.[33] The injected carrier density increases with the applied voltage until the traps are completely filled, leading to the sharp rise of the current (region III). The resulting trap-free SCLC regime is characterized by a quadratic Child's law (m ∼ 2) (region IV).[34−36]

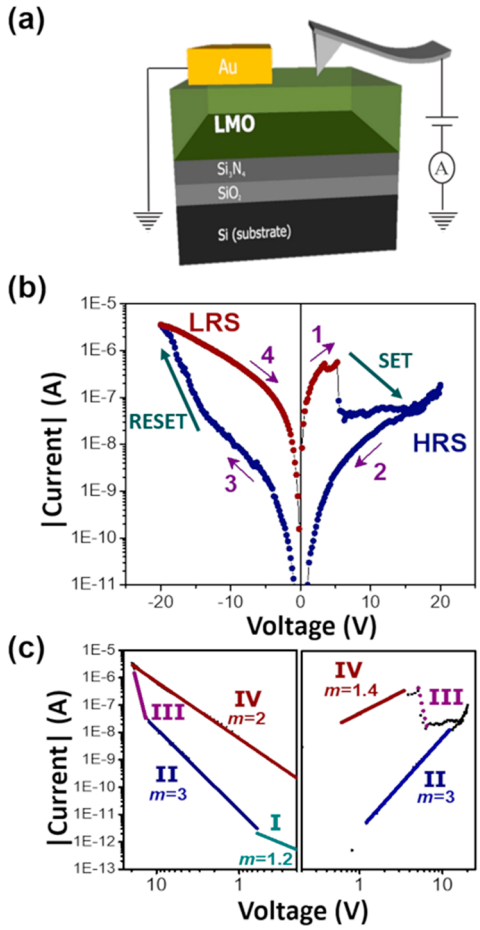

Figure 2. (a) Sketch of the top−top memristive device configuration, where the Au top electrode was grounded and the AFM tip on LMO thin film was biased. (b) I−V characteristics obtained for LMO in the described configuration. (c) Plot of $\log(I)$ vs $\log(V)$ for the positive applied voltage (right) and negative applied voltage (left) showing the different regime of the SCLC-like mechanism.

For positive voltage, the behavior is similar, except for certain differences in the slope in LRS ($m \neq 2$) and the absence of the ohmic regime. These differences can be explained by the nature of the p(degenerate)/p junction between the tip and the material, which is electron-blocking and hole-passing type when positively biased. A particular case was the first sweep, in which a first regime with a slope ca. 1.4 is observed when operating at low voltages. We can surmise that this electronic behavior results from the heterogeneous contact formed at the nanoscale between the LMO surface in its virgin state and the highly doped tip, i.e., contact between two materials with different carrier density.[31]

Thus, the resistive switching in our material can be described by a SCLC-like mechanism as a change of the transport regime from a trap-free to a trap-controlled SCLC, corresponding to the LRS and HRS, respectively. This behavior was corroborated by performing "read" measurements for both resistance states, i.e., I−V curves with small ranges of voltage (from 0 to 0.5 V). Section S.2 in the Supporting Information (Figures S4 and S5) presents more details of the I−V curves analysis for the multiple cycles conducted.

DOI: 10.1021/acsaelm.9b00030
ACS Appl. Electron. Mater. 2019, 1, 675−683

The ratio between the HRS and LRS was of ~10^2. Both resistance states were stable, and no change in resistance was observed after several days under different atmospheres, i.e., inside the glovebox, under UHV and in an air environment.

Pulse measurements varying the voltage magnitude were performed to optimize the SET and RESET voltages. After each pulse, the resistance value was read applying a V_{read} = 0.5 V pulse. For writing voltages lower than 3 V, there was no significant change in the value of resistance read after (not shown). However, as shown in Figure 3, the resistance

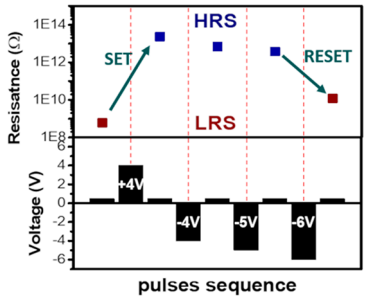

Figure 3. Pulse $I-V$ response on LMO surface: (top) the resistance read after each step with V_{read} = 0.5 V; (bottom) pulse sequence, pulse duration = 0.5 s.

increases by up to 4 orders of magnitude after applying a 4 V pulse for 0.5 s. On the other hand, we observe that a larger negative bias of −6 V was required to come back to the LRS state. The difference of behavior between negative and positive voltage is in agreement with the asymmetry observed in the $I-V$ responses. We were thus able to define two characteristic voltages V_{SET} = 4 V and V_{RESET} = −6 V, allowing reproducible switching between the two resistance states.

To selectively obtain switched micrometer-scale regions, a 3 × 3 μm^2 area of virgin LMO surface was scanned by c-AFM using these two characteristic voltages, defining two concentric squares at different resistance states. The resulting resistance map is represented in Figure 4a, where three different regions are observed: (i) the virgin surface, (ii) an outer square of 3 × 3 μm^2 at HRS where V_{SET} was applied, and (iii) an inner square of 1 × 1 μm^2 at LRS where V_{SET} and V_{RESET} were consecutively applied. Figure 4b shows a 0.5 μm large averaged resistance profile extracted from the dotted green line crossing the scanned surface (see Figure 4a). The first micrometers correspond to the virgin region, which was at initial LRS. After 2 μm, the resistance changes along the concentric squares are observed. In the central region, a LRS with a resistance value close to the initial one was attained, confirming the HRS/LRS ratio of 10^2 and the possibility of obtaining reversible switching also in the scanning mode. As shown, in LMO the changes in resistance occur mainly below the tip and laterally (horizontally) for a radius of ~100 nm around the tip. No modifications were observed in the region between the tip and Au electrode for larger distances.

Physicochemical Modification of the Surface. Being able to selectively obtain micrometer-scale regions at different resistance states opens the way to various relevant characterization studies to investigate the corresponding surface chemistry and electronic structure. To this end the chemical changes of the surface were probed by XPEEM by performing local spectroscopic measurements in 30 × 30 μm^2 HRS and virgin regions. The core level spectra of each LMO

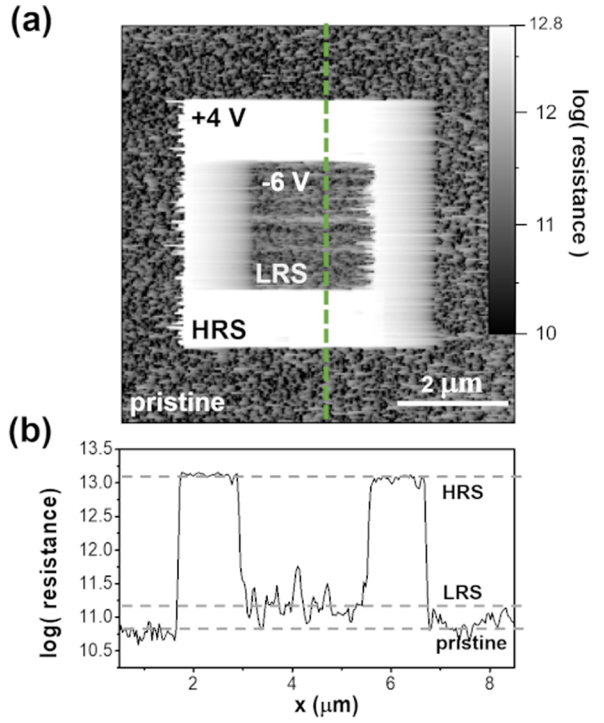

Figure 4. (a) Resistance map of the LMO surface after defining two concentric squares at different resistance states by c-AFM, i.e., an outer square at HRS and an inner square at LRS. (b) Resistance profile taken along the green dashed line, detailing the different resistance states.

component, i.e., O 1s, La $3d_{5/2}$, and Mn 3s, of the two regions (virgin and HRS) are shown in Figure 5. It is noteworthy to mention that in this work only the La $3d_{5/2}$ core level is presented because the other spin−orbit La $3d_{3/2}$ component overlaps with the Auger La $M_{4,5}N_{4,5}N_{4,5}$ peak.

The O 1s spectrum consists of two contributions. Although many studies on perovskite oxides assign these two contributions to "bulk" and "surface" oxygen,[37] given the high surface sensitivity of the XPEEM technique (~4 nm), we consider it more accurate to label the low binding energy component as "subsurface" LMO (instead of bulk) and the high binding energy component as "surface" oxygen. The first contribution corresponds to the oxygen of the first atomic layers of the material which may not have the same environment as the bulk ones, whereas the second contribution can come from oxygen compounds adsorbed on the surface (such as water, hydrocarbon contamination, etc.) or due to a drift of the perovskite oxygen from the LMO subsurface to the surface. In this sense, oxygen movement from the subsurface to the surface was observed in other oxides using ^{18}O tracking,[38] and singly negatively charged oxygen (O^-) has been shown to be thermodynamically stable as an adsorbed specie on the surface of transition-metal oxides.[39]

In the virgin state (LRS, top line of Figure 5), the main contribution to the O 1s core level corresponds to the doubly negatively charged O^{2-} ions from the LMO subsurface. After the resistance change, a strong increase of the surface contribution is observed in the HRS region. Because resistive switching was induced in a very low oxygen partial pressure atmosphere, the surface oxygen necessarily comes, mostly, from the LMO material itself. This is in agreement with the

DOI: 10.1021/acsaelm.9b00030
ACS Appl. Electron. Mater. 2019, 1, 675−683

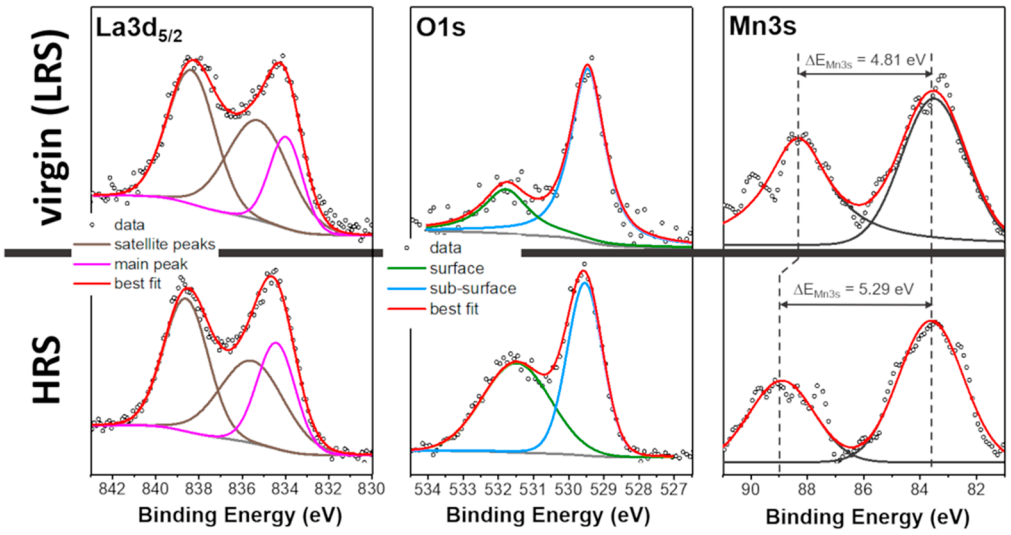

Figure 5. XPEEM analysis of the La $3d_{5/2}$, O 1s, and Mn 3s core levels of the LMO surface. The top row corresponds to a virgin region and the bottom row after applying −10 V by c-AFM (HRS).

relative elemental concentrations in the LMO matrix as determined by the compositional analysis (see Table1).

Table 1. Results of XPS Quantification in the Two Resistance State Regions (LRS and HRS)

	LRS			HRS		
element	La	Mn	O	La	Mn	O
rel concn (%)	16	18	66	20	21	59

Note that only the subsurface contribution is considered for the oxygen quantification since the surface contribution arises from oxygen atoms adsorbed on the interface, i.e., outside the lattice. A closer analysis of the O 1s spectrum shows that the composition of the virgin surface (in LRS) presents an excess of oxygen, as expected for the $LaMnO_{3+\delta}$ films, whereas in the HRS region the composition is approximately the one of stoichiometric $LaMnO_{3.0}$ ($\delta = 0$), which means that the material has been reduced (by a valence change of the Mn cation, since La possesses a very stable 3+ oxidation state). Even more interestingly, because of the increase of the surface contribution, the total oxygen amount is maintained constant in both cases, which indicates that the oxygen removed from the subsurface remains adsorbed on the surface instead of being expelled. This oxygen movement is driven by the positive bias applied on the surface by the AFM tip following the electric field lines. The sharp SET is thus related to a chemical reduction process leading to the formation of a depletion region, which would be governed by the SCLC-like mechanism, as observed in the LMO switching characteristics.

The La 3d photoelectron peak of lanthanum compounds usually shows very prominent satellite features due to core−hole screening processes.[40−43] Indeed, after 3d ionization, the initially unoccupied 4f levels are pulled down close to the valence orbitals of the neighborhood, thus allowing charge transfer. This results in two possible configurations of the ionic system depending on whether the screening charge is transferred to a 4f orbital or not.[44] The resulting X-ray photoelectron spectrum is therefore a combination of those final states composed by a main peak without charge transfer (pink line in Figure 5) and two satellite peaks with charge transfer and bonding/antibonding states (gray lines in Figure 5).[45−47] In particular, for the La $3d_{5/2}$ core level component, the ratio between the main peak and the satellites is significantly different in the two regions. In the HRS spectrum, the relative intensity of the main peak increases compared to the LRS region. This is in good agreement with the removal of oxygen from LMO explained above, which leads to a diminution of the O 2p electron density. The reduction of the La surrounding environment leads to less favorable conditions for charge transfer and thus to a diminution of the satellite intensity.

The photoemission spectra of 3d transition-metal complexes such as Mn present various multiplet structures. Mn 3s core levels are split into two contributions. This 3s doublet occurs for the unfilled 3d transition-metal complexes and is due to the presence of two possible spin states, i.e., spin-up and spin-down, resulting on 3s photoemission with two different associated 3s3d electrostatic exchange interactions. The energy separation between the high-spin and the low-spin in the 3s core level signal may be expressed by the Van Vleck's theorem as[48]

$$\Delta E_{3s} = 0.2(n + 1)G^2(3s3d) \quad (1)$$

where n is the number of unpaired 3d electrons and G^2 the Slater exchange integral.

The energy separation increases linearly against n as long as the nature of the ligands is the same.[49] In this way, a linear relationship between ΔE_{3s} and the oxidation state of the transition metal has been demonstrated for simple oxides[50] and extended to mixed valence oxides (for instance, Mn^{2+}/Mn^{3+} in Mn_3O_4[51]). Data reported in the literature give an average multiplet splitting of 5.4 eV for pure Mn^{3+} and 4.4 eV for pure Mn^{4+}.[50,51] In the present work the initial value of the energy splitting in LRS is 4.81 eV, which is in between the values for Mn^{3+} and Mn^{4+}. This indicates the presence of a mixture of both valence states and confirms the nonstoichiometric nature of the virgin LMO thin films. By using eq 1, we calculate the Mn valence state in $LaMnO_{3+\delta}$ surface to be of 3.6. This Mn^{3+}/Mn^{4+} mixed valence is responsible for the electrical conduction properties at the LRS, where traps are filled and free charge carriers are transferred between Mn and O atoms. After the

DOI: 10.1021/acsaelm.9b00030
ACS Appl. Electron. Mater. 2019, 1, 675−683

resistance change, the energy splitting rises up to 5.29 eV. This latter value close to pure Mn^{3+} confirms the stoichiometry of LMO in HRS shown in Table 1. Hence, a decrease of the Mn^{4+} content leads to a drastic decrease of the electrical conductivity. Beyond the confirmation of the reduction occurring in LMO, we clearly demonstrate that the electrical properties of the films and charge neutrality during the switching response are provided by a change in the manganese oxidation state to accommodate the local nonstoichiometry caused by the oxygen ions movement. The corresponding redox reaction can be depicted by the following equation:

$$La_{1-x}\square_x(Mn^{3.6+})_y\square_{1-y}O_3(LRS) \rightleftharpoons La_{1-x}\square_x(Mn^{3.1+})_y\square_{1-y}O_{3-0.25} + 0.25O^{2-}(HRS)$$

with $\square$ being the cation vacancies.

Taking advantage of the strong Jahn−Teller (J−T) character of LMO, we focus here on elucidating the microstructural changes involved in the switching response. Micro-Raman spectroscopy was used to investigate the evolution of the J−T distortion in the same two areas (LRS and HRS). Figure 6 presents the most relevant region of the LMO Raman spectra (550−750 cm^{-1}), as a large part of the LMO signal is screened by the intense Raman signal arising from the Si substrate.

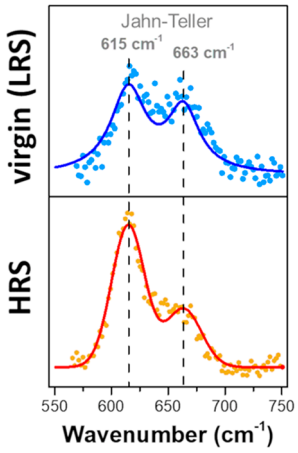

Figure 6. Raman spectra of the LMO film collected at room temperature in virgin and HRS regions (λ = 488 nm).

Both Raman spectra are composed by two lines at 615 and 663 cm^{-1} ascribed to the J−T distortion in rhombohedral LMO.[52,53] By comparing them, we observe an increase of the first contribution in the HRS region compared to the virgin one. As reported by Dubey and co-workers, this feature increases with decreasing oxygen content, thus increasing the concentration of Mn^{3+}.[54] This observation confirms the previous XPEEM results, which pointed out to a change in the Mn^{3+}/Mn^{4+} ratio between the two resistance states (lower Mn oxidation state for the HRS). Thus, it has been experimentally confirmed that the J−T distortion is enhanced by the presence of more Mn^{3+} in HRS. Considering that micro-Raman is a bulk sensitive characterization technique, these observations confirm the reduction of Mn^{4+} and clearly show that the space charge layer created by removing oxygen also causes important microstructural perturbations of the LMO lattice.

Complementarily, a series of photoelectron images across the photoemission threshold were acquired. Figure 7a presents the work function (WF) mapping obtained after integration of the series and correction of the analyzer nonisochromaticity. A contrast between the virgin surface and the 30 × 30 μm^2 HRS region is observed, indicating a clear difference in the WF value for the two resistance states. As depicted in Figure 7b, the histogram extracted from the WF map shows two average values. The highest value (WF1 = 4.63 eV) comes from the virgin surface (LRS) and the lowest one (WF2 = 4.35 eV) from the HRS region. These values can be compared with the reported 4.5−5.1 eV range measured on various $LaMnO_3$ samples and the 5.21 eV calculated, paticularly, for a MnO_2 terminated surface.[55−58]

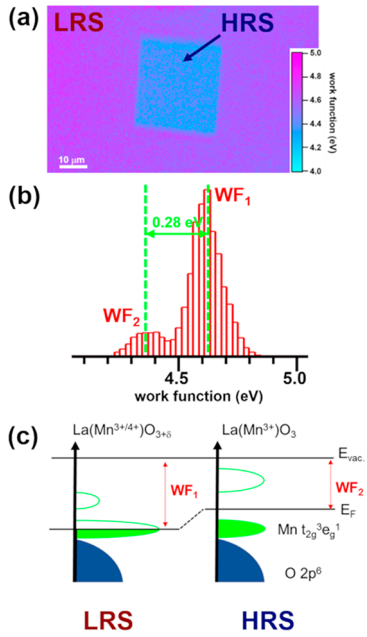

Figure 7. (a) Work function mapping of the LMO surface after the resistance has been locally changed by c-AFM. (b) Histogram showing the difference in work function. (c) Schematic DOS of partially filled 3d shell and the effect of removing oxygen from the LMO.

Figure 7c illustrates the schematic density of states diagrams of both HRS and LRS of our LMO films based on the model proposed by Jacobs et al. and Mellan et al.[58,59] The work function represented refers to the energy difference between vacuum and the highest filled electronic state of the valence band (which is not the same as the Fermi level) and may be different for semiconductor materials such as LMO. The screened states correspond to filled states. The diminution of the oxygen content and the reduction of the manganese oxidation state from $Mn^{3+/4+}$ to Mn^{3+} in HRS yields a slight decrease of the WF, indicating a shrinkage of the band hybridization (i.e., a smaller overlapping between Mn 3d and O 2p bands) which results in an upward shift of the Fermi level.[58] The distinct WF values measured at both resistance states are in accordance with the charge carrier transport properties previously described.

In summary, the combination of different advanced spectroscopic techniques allowed us to disentangle the physicochemical fingerprints related to the interfacial memristive behavior of LMO. The pristine LMO is characterized by the presence of a Mn^{3+}/Mn^{4+} mixture which ensures the electroneutrality of the material. Upon the application of positive bias, part of the oxygen is removed from the

DOI: 10.1021/acsaelm.9b00030
ACS Appl. Electron. Mater. 2019, 1, 675−683

subsurface to the surface, increasing the density of traps in the LMO and switching to HRS that is governed by a SCLC-like mechanism. Both the stoichiometry calculation and the Mn 3s splitting reveal that the surface composition is almost purely Mn^{3+}. Hence, we have proved that the increase of the resistance due to the movement of oxygen comes together with a Mn redox reaction to compensate the global charge, enhancing the Jahn−Teller effect by decreasing the Mn^{4+} concentration. Besides, we have demonstrated that by applying a negative electric field to the surface, oxygen is gradually reincorporated into the LMO both from the adsorbed surface and from the surrounding LMO oxide. The amount of adsorbed oxygen is very similar to the oxygen removed during the SET stage, which explains the resistance value after the RESET is the same as for the virgin state.

CONCLUSION

In this work we have demonstrated that the resistance of a $LaMnO_{3+\delta}$ thin film can be reversibly changed within a range of 2 orders of magnitude using c-AFM. The possibility of changing the resistance state in a spatially defined region allowed us to combine several complementary characterization techniques to investigate the mechanism involved in the RS response. The XPEEM measurements highlight the diminution of the oxygen content in the LMO subsurface is correlated to the resistance increase. Interestingly, the oxygen is not expelled from the material but remains adsorbed on the surface, allowing the reverse process to occur. This loss of oxygen has a direct influence both on the Mn valence, which goes from 3.6 to 3.1, and on the work function that decreases by 0.28 eV. The initial presence of cation vacancies is then compensated by the apparition of oxygen vacancies, resulting in a rise of the Fermi level. We also explained the $I-V$ characteristics measured by c-AFM in agreement with a space-charge-limited conduction mechanism relating them with the physicochemical changes observed. In HRS, the current is strongly controlled by the presence of traps at the subsurface resulting from the extraction of oxygen under positive bias. These traps are filled when oxygen is reincorporated into the subsurface, leading to a trap-free SCLC-like mechanism. Globally these results give a complete and comprehensive picture of the mechanisms involved in interfacial resistive switching occurring at the surface of $LaMnO_{3+\delta}$ thin films.

ASSOCIATED CONTENT

Supporting Information

The Supporting Information is available free of charge on the ACS Publications website at DOI: 10.1021/acsaelm.9b00030.

Complementary thin film characterization by SEM and TEM; retention and endurance measured by c-AFM; reproducibility of the SCLC-like mechanism; and resistance mapping using different SET voltage (PDF)

AUTHOR INFORMATION

Corresponding Authors

*(B.M.) E-mail Meunier.Ben@outlook.com.
*(M.B.) E-mail Monica.Burriel@grenoble-inp.fr.

ORCID

Benjamin Meunier: 0000-0001-5178-6427

Notes

The authors declare no competing financial interest.

ACKNOWLEDGMENTS

The authors thank Laetitia Rapenne and Florence Robaut for TEM observations and EIB lamella preparation. This work has been supported by the ANR funded project “Alps Memories” (ANR-15-CE24-0018). Facilities of the NanoCharacterisation PlatForm (PFNC) used in this work are supported by the “Recherches Technologiques de Base” Program of the French Ministry of Research. This project has received funding from the European Union’s Horizon 2020 research and innovation program under the Marie Skłodowska-Curie Grant Agreement No. 746648 - PerovSiC (for D.P.).

ABBREVIATIONS

LMO, $LaMnO_{3+\delta}$; HRS, high resistance state; LRS, low resistance state; VCM, valence change mechanism; SCLC, space-charge-limited conduction; WF, work function.

REFERENCES

(1) Lai, S. Flash Memories: Successes and Challenges. *IBM J. Res. Dev.* **2008**, *52*, 529−535.

(2) Grupp, L. M.; Davis, J. D.; Swanson, S. The Bleak Future of NAND Flash Memory. Proceedings of the 10th USENIX Conference on File and Storage Technologies, 2012.

(3) Waser, R.; Aono, M. Nanoionics-Based Resistive Switching Memories. *Nat. Mater.* **2007**, *6*, 833.

(4) Kim, D. S.; Kim, Y. H.; Lee, C. E.; Kim, Y. T. Colossal Electroresistance Mechanism in a Au/Pr0.7Ca0.3MnO3/Pt Sandwich Structure: Evidence for a Mott Transition. *Phys. Rev. B: Condens. Matter Mater. Phys.* **2006**, *74*, 174430.

(5) Shi, J.; Ha, S. D.; Zhou, Y.; Schoofs, F.; Ramanathan, S. A Correlated Nickelate Synaptic Transistor. *Nat. Commun.* **2013**, *4*, 3676.

(6) Weston, I.; Janotti, A.; Cui, X. Y.; Himmetoglu, B.; Stampfl, C.; Van de Walle, C. G. Structural and Electronic Properties of $SrZrO_3$ and $Sr(Ti,Zr)O_3$ Alloys. *Phys. Rev. B: Condens. Matter Mater. Phys.* **2015**, *92*, No. 085201.

(7) Kim, D. S.; Lee, C. E.; Kim, Y. H.; Kim, Y. Y. Effect of Oxygen Annealing on $Pr_{0.7}Ca_{0.3}MnO_3$ Thin Film for Colossal Electroresistance at Room Temperature. *J. Appl. Phys.* **2006**, *100* (9), 093901.

(8) Liu, S. Q.; Wu, N. J.; Ignatiev, A. Electric-Pulse Induced Reversible Change Effect in Magnetoresistive Films. *Appl. Phys. Lett.* **2000**, *76*, 2749.

(9) Gonzalez-Rosillo, J. C.; Ortega-Hernandez, R.; Jareño-Cerulla, J.; Miranda, E.; Suñe, J.; Granados, X.; Obradors, X.; Palau, A.; Puig, T. Volume Resistive Switching in Metallic Perovskite Oxides Driven by the Metal-Insulator Transition. *J. Electroceram.* **2017**, *39*, 185.

(10) Moreno, C.; Munuera, C.; Valencia, S.; Kronast, F.; Obradors, X.; Ocal, C. Reversible Resistive Switching and Multilevel Recording in La0.7Sr0.3MnO3 Thin Films for Low Cost Nonvolatile Memories. *Nano Lett.* **2010**, *10*, 3828−3835.

(11) Szot, K.; Speier, W.; Bihlmayer, G.; Waser, R. Switching the Electrical Resistance of Individual Dislocations in Single-Crystalline $SrTiO_3$. *Nat. Mater.* **2006**, *5*, 312−320.

(12) Waser, R.; Dittmann, R.; Staikov, G.; Szot, K. Redox-Based Resistive Switching Memories − Nanoionic Mechanisms, Prospects, and Challenges. *Adv. Mater.* **2009**, *21*, 2632.

(13) Bagdzevicius, S.; Maas, K.; Boudard, M.; Burriel, M. Interface-Type Resistive Switching in Perovskite Materials. *J. Electroceram.* **2017**, *39*, 157.

(14) Kubicek, M.; Schmitt, R.; Messerschmitt, F.; Rupp, J. L. M. Uncovering Two Competing Switching Mechanisms for Epitaxial and Ultrathin Strontium Titanate-Based Resistive Switching Bits. *ACS Nano* **2015**, *9* (11), 10737−10748.

(15) Dittmann, R.; Muenstermann, R.; Krug, I.; Park, D.; Menke, T.; Mayer, J.; Besmehn, A.; Kronast, F.; Schneider, C. M.; Waser, R.

Scaling Potential of Local Redox Processes in Memristive SrTiO3 Thin-Film Devices. *Proc. IEEE* **2012**, *100* (6), 1979.
(16) Herpers, A.; Lenser, C.; Park, C.; Offi, F.; Borgatti, F.; Panaccione, G.; Menzel, S.; Waser, R.; Dittmann, R. Spectroscopic Proof of the Correlation between Redox-State and Charge-Carrier Transport at the Interface of Resistively Switching Ti/PCMO Devices. *Adv. Mater.* **2014**, *26*, 2730−2735.
(17) Arndt, B.; Borgatti, F.; Offi, F.; Phillips, M.; Parreira, P.; Meiners, T.; Menzel, S.; Skaja, K.; Panaccione, G.; MacLaren, D. A.; Waser, R.; Dittmann, R. Spectroscopic Indications of Tunnel Barrier Charging as the Switching Mechanism in Memristive Devices. *Adv. Funct. Mater.* **2017**, *27*, 1702282.
(18) Baeumer, C.; Schmitz, C.; Marchewka, A.; Mueller, D. N.; Valenta, R.; Hackl, J.; Raab, N.; Rogers, S. P.; Khan, M. I.; Nemsak, S.; Shim, M.; Menzel, S.; Schneider, C. M.; Waser, R.; Dittmann, R. Quantifying Redox-Induced Schottky Barrier Variations in Memristive Devices via *In Operando* Spectromicroscopy with Graphene Electrodes. *Nat. Commun.* **2016**, *7*, 12398.
(19) Baeumer, C.; Schmitz, C.; Ramadan, A. H. H.; Du, H.; Skaja, K.; Feyer, V.; Müller, P.; Arndt, B.; Jia, C. L.; Mayer, J.; De Souza, R. A.; Schneider, C. M.; Waser, R.; Dittmann, R. Spectromicroscopic Insights for Rational Design of Redox-Based Memristive Devices. *Nat. Commun.* **2015**, *6*, 8610.
(20) Yao, L.; Inkinen, S.; van Dijken, S. Direct Observation of Oxygen Vacancy-driven Structural and Resistive Phase Transitions in $La_{2/3}Sr_{1/3}MnO_3$. *Nat. Commun.* **2017**, *8*, 14544.
(21) Töpfer, J.; Goodenough, J. B. $LaMnO_{3+\delta}$ Revisited. *J. Solid State Chem.* **1997**, *130*, 117−128.
(22) Coey, J. M. D.; Viret, M.; Von Molnár, S. Mixed-Valence Manganites. *Adv. Phys.* **1999**, *48* (2), 167−293.
(23) Ge, C.; Jin, K.-J.; Gu, L.; Peng, L.-C.; Hu, Y.-S.; Guo, H.-Z.; Shi, H.-F.; Li, J.-K.; Wang, J. O.; Guo, X.-X.; Wang, C.; He, M.; Lu, H.-B.; Yang, G.-Z. Metal-Insulator Transition Induced by Oxygen Vacancies from Electrochemical Reaction in Ionic Liquid-Gated Manganite Films. *Adv. Mater. Interfaces* **2015**, *2*, 1500407.
(24) Feng, Y.; Jin, K.-J.; Gu, L.; He, X.; Ge, C.; Zhang, Q.-H.; He, M.; Guo, Q.-L.; Wan, Q.; He, M.; Lu, H.-B.; Yang, G. Insulating Phase at Low Temperature in Ultrathin $La_{0.8}Sr_{0.2}MnO_3$ Films. *Sci. Rep.* **2016**, *6*, 22382.
(25) Jiang, S. P. Development of Lanthanum Strontium Manganite Perovskite Cathode Materials of Solid Oxide Fuel Cells: a review. *J. Mater. Sci.* **2008**, *43*, 6799−6833.
(26) Tofield, B. C.; Scott, W. R. Oxidative Nonstoichiometry in Perovskites, an Experimental Survey; the Defect Structure of an Oxidized Lanthanum Manganite by Powder Neutron Diffraction. *J. Solid State Chem.* **1974**, *10*, 183−194.
(27) Van Roosmalen, J. A. M.; Cordfunke, E. H. P. The Defect Chemistry of $LaMnO_{3\pm\delta}$. *J. Solid State Chem.* **1994**, *110*, 106−108.
(28) Van Roosmalen, J. A. M.; Van Vlaanderen, P.; Cordfunke, E. H. P. Phases in the Perovskite-Type $LaMnO_{3+\delta}$ Solid Solution and the La_2O_3-Mn_2O_3 Phase Diagram. *J. Solid State Chem.* **1995**, *114*, 516−523.
(29) Scofield, J. H. Theoretical Photoionization Cross Sections From 1 to 1500 keV, Report No. UCRL-51326, Lawrence Livermore Laboratory, University of California, Livermore, CA, 2013.
(30) Rodriguez-Lamas, R.; Pla, D.; Chaix-Pluchery, O.; Meunier, B.; Wilhelm, F.; Rogalev, A.; Rapenne, L.; Mescot, X.; Rafhay, Q.; Roussel, H.; Boudard, M.; Jiménez, C.; Burriel, M. Integration of $LaMnO_{3+\delta}$ Films on Platinized Silicon Substrates for Resistive Switching Applications by PI-MOCVD. *Beilstein J. Nanotechnol.* **2019**, *10*, 389−398.
(31) Esposito, V.; Garbayo, I.; Linderoth, S.; Pryds, N. In *Epitaxial Growth of Complex Metal Oxides*; Koster, G., Huijben, M., Rijnders, G., Eds.; Elsevier: 2015; pp 443−478.
(32) Chiu, F. C. A Review on Conduction Mechanisms in Dielectric Films. *Adv. Mater. Sci. Eng.* **2014**, *2014*, 578168.
(33) Grove, S. A. In *Physics and Technology of Semiconductor Devices*; Wiley: New York, 1967.
(34) Lim, E. W.; Ismail, R. Conduction Mechanism of Valence Change Resistive Switching Memory: A Survey. *Electronics* **2015**, *4*, 586−613.
(35) Shang, D. S.; Wang, Q.; Chen, L. D.; Dong, R.; Li, X. M.; Zhang, W. Q. Effect of Carrier Trapping on the Hysteretic Current-Voltage Characteristics in $Ag/La_{0.7}Ca_{0.3}MnO_3/Pt$ Heterostructures. *Phys. Rev. B: Condens. Matter Mater. Phys.* **2006**, *73*, 245427.
(36) Zhu, Y. B.; Ang, L. K. Non-uniform Space Charge Limited Current Injection into a Nano Contact Solid. *Sci. Rep.* **2015**, *5*, 9173.
(37) Fierro, J. L. G.; Tejuca, L. G. Non-Stoichiometric Surface Behaviour of $LaMnO_3$ Oxides as Evidenced by XPS. *Appl. Surf. Sci.* **1987**, *27*, 453−457.
(38) Yoshida, C.; Kinoshita, K.; Yamasaki, T.; Sugiyama, Y. Direct Observation of Oxygen Movement During Resistance Switching in NiO/Pt Film. *Appl. Phys. Lett.* **2008**, *93*, No. 042106.
(39) Bielanski, A.; Haber, J. Oxygen in Catalysis on Transition Metal Oxides. *Catal. Rev.: Sci. Eng.* **1979**, *19*, 1.
(40) Wertheim, G. K.; Rosencwaig, A.; Cohen, R. L.; Guggenheim, H. J. Multiplet Splitting of the 4s and 5s Electrons of Rare Earths. *Phys. Rev. Lett.* **1971**, *27*, 505.
(41) Jorgensen, C. K.; Berthou, H. Split Photo-Electron Signals from the Unique Closed-Shell Cation Lanthanum(III). *Chem. Phys. Lett.* **1972**, *13*, 186.
(42) Signorelli, A. J.; Hayes, R. G. X-Ray Photoelectron Spectroscopy of Various Core Levels of Lanthanum Ions: The Roles of Monopole Excitation and Electrostatic Coupling. *Phys. Rev. B* **1973**, *8* (1), 81.
(43) Suzuki, S.; Ishii, T.; Sagawa, T. X-Ray Photoemission Spectra of 4d and 3d Electrons in Lanthanum- and Cerium-Halides. *J. Phys. Soc. Jpn.* **1974**, *37*, 1334−1340.
(44) Wendin, G. In *Structure and Bondings 45*; Springer-Verlag: 1981.
(45) Kotani, A.; Okada, M.; Jo, T.; Bianconi, A.; Marcelli, A.; Parlebas, J. C. Many Body Effect in inner Shell Photoemission and Photoabsorption Specrta of La Compounds. *J. Phys. Soc. Jpn.* **1987**, *56*, 798−809.
(46) Park, K.-H.; Oh, S.-J. Electron-Spectroscopy Study of Rare-Earth Trihalides. *Phys. Rev. B: Condens. Matter Mater. Phys.* **1993**, *48*, 14833−14842.
(47) Sunding, M. F.; Hadidi, K.; Diplas, S.; Lovvik, O. M.; Norby, T. E.; Gunnæs, A. E. XPS Characterization of In Situ Treated Lanthanum Oxide and Hydroxide Using Tailored Charge Referencing and Peak Fitting Procedures. *J. Electron Spectrosc. Relat. Phenom.* **2011**, *184*, 399−409.
(48) Van Vleck, J. H. The Dirac Vector Model in Complex Spectra. *Phys. Rev.* **1934**, *45*, 405.
(49) Kozakov, A. T.; Kochur, A. G.; Googlev, K. A.; Nikolskii, A. V.; Torgashev, V. I.; Trotsenko, V. G.; Bush, A. A. Valence State of Manganese and Iron in $La_{1-x}A_xMnO_3$ (A = Ca, Sr) and $Bi_{1-x}Sr_xFeO_3$ Systems from Mn2p, Mn3s, Fe2p and Fe3s X-ray Photoelectron Spectra. Effect of Delocalization on Fe3s Spectra Splitting. *J. Alloys Compd.* **2015**, *647*, 947−955.
(50) Ilton, E. S.; Post, J. E.; Heaney, P. J.; Ling, F. T.; Kerisit, S. N. XPS Determination of Mn Oxidation States in Mn (Hydr)Oxides. *Appl. Surf. Sci.* **2016**, *366*, 475−485.
(51) Galakhov, V. R.; Demeter, M.; Bartkowski, S.; Neumann, M.; Ovechkina, N. A.; Kurmaev, E. Z.; Lobachevskaya, N. I.; Mukovskii, Y. M.; Mitchell, J.; Ederer, D. L. Mn 3s Exchange Splitting in Mixed-Valence Manganites. *Phys. Rev. B: Condens. Matter Mater. Phys.* **2002**, *65*, 113102.
(52) Abrashev, M. V.; Litvinchuk, A. P.; Iliev, M. N.; Meng, R. L.; Popov, V. N.; Ivanov, V. G.; Chakalov, R. A.; Thomsen, C. Comparative Study of Optical Phonons in the Rhombohedrally Distorted Perovskites $LaAlO_3$ and $LaMnO_3$. *Phys. Rev. B: Condens. Matter Mater. Phys.* **1999**, *59*, 4146.
(53) Iliev, M. N.; Abrashev, M. V. Raman Phonons and Raman Jahn-Teller bands in Perovskite-like Manganites. *J. Raman Spectrosc.* **2001**, *32*, 805−811.

DOI: 10.1021/acsaelm.9b00030
ACS Appl. Electron. Mater. 2019, 1, 675−683

(54) Dubey, A.; Sathe, V. G.; Rawat, R. Signature of Jahn-Teller Distortion and Oxygen Stoichiometry in Raman Spectra of Epitaxial LaMnO3+ Thin Films. *J. Appl. Phys.* **2008**, *104*, 113530.
(55) Kida, T.; Guan, G.; Yoshida, A. $LaMnO_3$/CdS Nanocomposite: a New Photocatalyst for Hydrogen Production from Water under Visible Light Irradiation. *Chem. Phys. Lett.* **2003**, *371*, 563.
(56) Stoerzinger, K. A.; Risch, M.; Suntivich, J.; Lu, W. M.; Zhou, J.; Biegalski, M. D.; Christen, H. M.; Ariando; Venkatesan, T.; Shao-Horn, Y. Oxygen Electrocatalysis on (001)-Oriented Manganes Perovskite Films: Mn Valency and Charge Transfer at the Nanoscale. *Energy Environ. Sci.* **2013**, *6*, 1582.
(57) Hong, H. T.; Stoerzinger, K. A.; Moritz, B.; Devereaux, T. P.; Yang, W.; Shao-Horn, Y. Probing LaMnO2 Metal and Oxygen Partial Density of States Using X-ray Emission, Absorption, and Photoelectron Spectroscopy. *J. Phys. Chem. C* **2015**, *119*, 2063.
(58) Jacobs, R.; Booske, J.; Morgan, D. Understanding and Controlling the Work Function of Perovskite Oxides using Density Functional Theory. *Adv. Funct. Mater.* **2016**, *26* (30), 5471−5482.
(59) Mellan, T. A.; Cora, F.; Grau-Crespo, R.; Ismail-Beigi, S. Importance of Anisotropic Coulomb Interaction in $LaMnO_3$. *Phys. Rev. B: Condens. Matter Mater. Phys.* **2015**, *92*, No. 085151.

DOI: 10.1021/acsaelm.9b00030
ACS Appl. Electron. Mater. 2019, 1, 675−683